

Sulfated Zirconium Metal–Organic Frameworks as Well-Defined Supports for Enhancing Organometallic Catalysis

Zoha H. Syed, Mohammad Rasel Mian, Roshan Patel, Haomiao Xie, Zihan Pengmei, Zhihengyu Chen, Florencia A. Son, Timothy A. Goetjen, Alon Chapovetsky, Kira M. Fahy, Fanrui Sha, Xingjie Wang, Selim Alayoglu, David M. Kaphan, Karena W. Chapman, Matthew Neurock, Laura Gagliardi, Massimiliano Delferro,* and Omar K. Farha*



Cite This: *J. Am. Chem. Soc.* 2022, 144, 16883–16897



Read Online

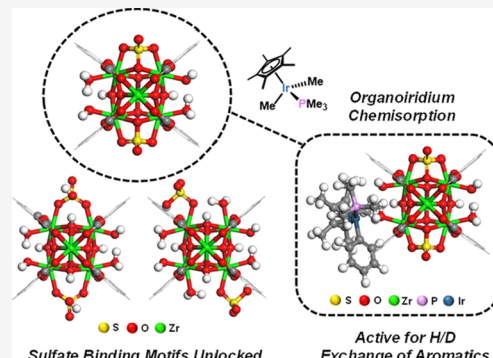
ACCESS |

Metrics & More

Article Recommendations

Supporting Information

ABSTRACT: Understanding heterogeneous catalysts is a challenging pursuit due to surface site nonuniformity and aperiodicity in traditionally used materials. One example is sulfated metal oxides, which function as highly active catalysts and as supports for organometallic complexes. These applications are due to traits such as acidity, ability to act as a weakly coordinating ligand, and aptitude for promoting transformations via radical cation intermediates. Research is ongoing about the structural features of sulfated metal oxides that imbue the aforementioned properties, such as sulfate geometry and coordination. To better understand these materials, metal–organic frameworks (MOFs) have been targeted as structurally defined analogues. Composed of inorganic nodes and organic linkers, MOFs possess features such as high porosity and crystallinity, which make them attractive for mechanistic studies of heterogeneous catalysts. In this work, Zr_6 -based MOF NU-1000 is sulfated and characterized using techniques such as single crystal X-ray diffraction in addition to diffuse reflectance infrared Fourier transform spectroscopy (DRIFTS). The dynamic nature of the sulfate binding motif is found to transition from monodentate, to bidentate, to tridentate depending on the degree of hydration, as supported by density functional theory (DFT) calculations. Heightened Brønsted acidity compared to the parent MOF was observed upon sulfation and probed through trimethylphosphine oxide physisorption, ammonia sorption, in situ ammonia DRIFTS, and DFT studies. With the support structure benchmarked, an organoiridium complex was chemisorbed onto the sulfated MOF node, and the efficacy of this supported catalyst was demonstrated for stoichiometric and catalytic activation of benzene- d_6 and toluene with structure–activity relationships derived.



INTRODUCTION

Approximately 80% of industrial chemical syntheses implement heterogeneous catalysis to generate commodity chemicals.¹ Nonetheless, the acquisition of mechanistic insights into the function and structure of heterogeneous catalysts is challenging but critical for improving catalytic activity.^{1–4} Investigations into speciation and derivation of structure–activity relationships are complicated by the irregular structures that define traditional, metal oxide-based heterogeneous catalysts. In contrast, homogeneous catalysts are known for highly tunable coordination spheres and are amenable to a host of characterization techniques, although recyclability can be challenging.^{1–4}

Integrating beneficial aspects of both types of the aforementioned catalysts, surface organometallic chemistry (SOMC) is a promising methodology.^{1–4} In this approach, solid-state support materials that are germane to classical heterogeneous catalysis, such as zirconia (ZrO_2), silica (SiO_2), or alumina (Al_2O_3), are used to anchor molecular coordination complexes. A reactive, single-site, supported species is formed

that can participate in a wide array of industrially relevant chemical transformations, such as hydrogenation,^{5–10} dehydrogenation,^{10–15} and polymerization,^{5,6,12,16–19} among numerous others.^{1–4} In the same vein, modified metal oxides have drawn attention for SOMC as stereoelectronic control over the reactivity of catalytically active sites can be exerted via support modification.^{1–4}

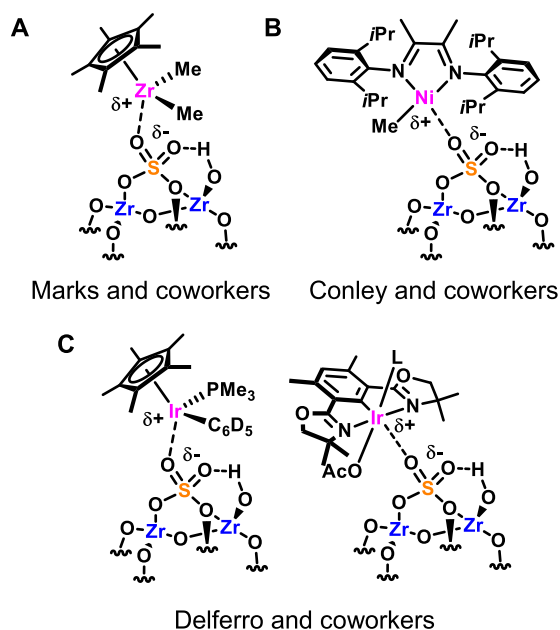
Notably, sulfated zirconia (SO_4/ZrO_2 , SZ)^{20–25} has been employed in a variety of contexts, both as a material with intrinsic catalytic activity for kinetically challenging reactions^{24,26–32} and as a catalyst support for C–H and C–C bond functionalization using early (Scheme 1A) and late

Received: May 18, 2022

Published: September 12, 2022



Scheme 1. SOMC of Early and Late Transition Metal Complexes Immobilized on Sulfated Zirconia



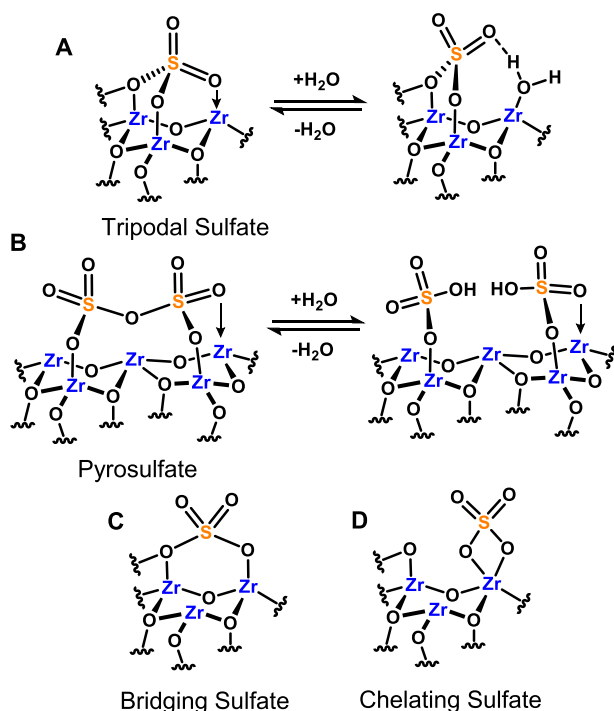
transition metals (**Scheme 1B,C**).^{1–4} For the latter, SO_4/ZrO_2 is thought to act as a weakly coordinating anion in the first coordination sphere of an organometallic complex upon grafting by analogy to noncoordinating molecular ligands such as triflate, tetrafluoroborate, or hexafluorophosphate.¹ As a result, the electrophilicity of grafted metal centers can be enhanced, rendering them more catalytically active for chemical bond activation compared to their unsupported counterparts.

The ability to function as a noncoordinating counterion is posited to stem from the surface structure and acidity of SO_4/ZrO_2 , though both are the topic of ongoing debate in the literature.^{23–25,30,35} In some contexts,^{21–23,36–39} it is hypothesized that “superacidic” Brønsted acid sites are present. Alternatively, others have touted the strong Lewis acidity of SO_4/ZrO_2 as the basis of its catalytic efficacy or its radical character.^{20,23,24,32,35,37,39–41}

Consequently, inquiries into sulfate binding motifs in the SO_4/ZrO_2 platform have been conducted to determine the premise of its properties. While countless structures, with varying degrees of hydration and connectivity, are thought to exist in SO_4/ZrO_2 (**Scheme 2**),^{20–32,35,37–41} two candidates remain the most pervasive. In one scenario, the sulfate (SO_4^{2-}) adopts a dehydrated tripodal configuration, interacting with three Zr sites on the surface (**Scheme 2A**).^{20,21,24,25,30,37,38,41} In a second scenario, two adjacent sulfate groups condense on the surface to form a bridging, pyrosulfate ($\text{S}_2\text{O}_7^{2-}$) species (**Scheme 2B**).^{20,34,37,38,42} In both cases, the sulfate groups are highly susceptible to hydration (**Scheme 2A,B**).

To address the questions that still exist about SO_4/ZrO_2 , a more tunable, a well-defined structure that is analogous to a metal oxide is desirable. One type of material that could serve such a purpose is the metal–organic framework (MOF).^{43–45} Composed of inorganic, metal cluster “nodes”, and multitopic organic “linkers,” MOFs are defined by crystallinity (a consequence of periodic structure), high porosity, and customizability. Accordingly, MOFs are employed in a myriad of applications, including catalysis.^{43–45} Structural parallels to

Scheme 2. Structural Binding Motifs Hypothesized to be Present in Sulfated Zirconia



bulk oxide catalyst supports can be seen in the nanoscale MOF node. The node is typically metal oxide-based (most commonly Zr)^{43–45} and possesses similar topological features to bulk metal oxides, such as Brønsted acidic hydroxyl- and aqua-ligands, in addition to tetravalent, metal-based Lewis acid sites. Thus, a sulfated MOF could function as an analogue to SO_4/ZrO_2 and provide information about the metal oxide and its efficacy for applications such as SOMC.

In seminal work by Yaghi and co-workers,^{46,47} a 6-connected $\text{Zr}_6\text{-b-a-s-e-d MOF}$, MOF-808 ($\text{Zr}_6\text{O}_5(\text{OH})_3(\text{BTC})_2(\text{HCOO})_5(\text{H}_2\text{O})_2$, $\text{BTC}^{3-} = 1,3,5\text{-benzenetricarboxylate}$) was treated with aqueous sulfuric acid to create MOF-808-SO_4 which had 2.5 sulfate groups installed per Zr_6 node. This sulfated MOF was found to possess strong Brønsted acid sites and could facilitate a variety of acid-catalyzed transformations.^{46,47} A mixture of species was found by single crystal X-ray diffraction (SCXRD). Upon thermal evacuation, the sulfate transitioned exclusively to the “chelating” mode, as confirmed by Rietveld refinement of powder X-ray diffraction (PXRD) patterns. This was hypothesized as the source of Brønsted acidity in MOF-808-SO_4 through its hydrogen bonding interaction with an adjacent $\text{Zr}-\text{OH}_2$ moiety on the node.⁴⁷ Others have undertaken similar studies with sulfated MOFs, probing the validity of the proposed “chelating” sulfate model in MOF-808-SO_4 ⁴⁸ and exploring properties of alternative sulfated MOFs.^{49–53}

While the chelating sulfate geometry has been proposed on bulk sulfated zirconia, other commonly proposed geometries have not yet been observed in MOFs, which we sought to investigate. In addition, while a shift in sulfate-binding has been shown to occur in a MOF-based system, we performed a deeper audit to discern structural evolution, such as hydration pathways, occurring in sulfated zirconia. Furthermore, the insights gained via MOFs about SO_4/ZrO_2 have not been applied toward SOMC, a field that invokes sulfated supports as

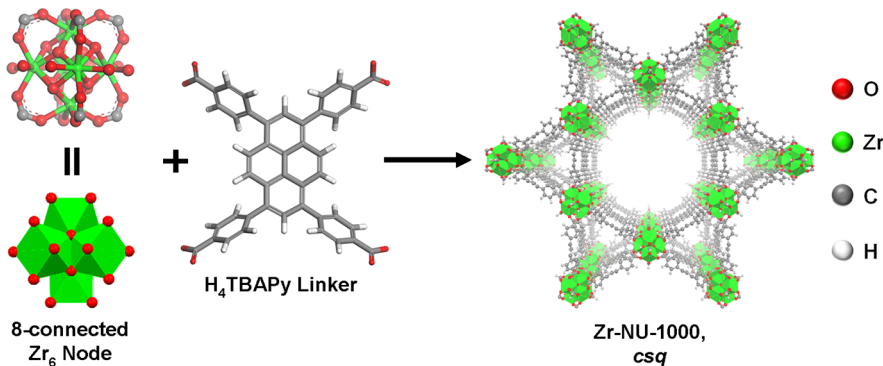


Figure 1. Zr-NU-1000 is composed of 8-connected, inorganic Zr_6 nodes and tetratopic H_4TBAPy organic linkers, which assemble to give a mesoporous MOF with *csq* topology.

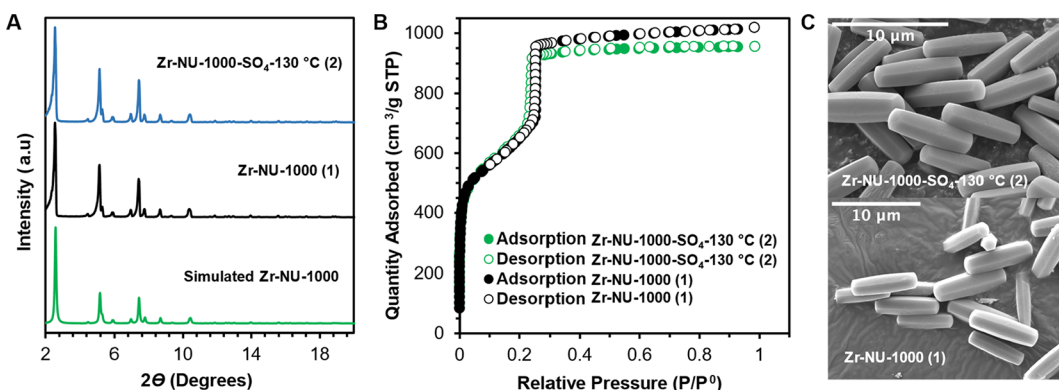


Figure 2. Comparison of **2** to parent MOF **1** to gauge structural integrity, (A) crystallinity and phase purity are maintained upon sulfation, as evidenced by similar PXRD patterns for **1** and **2**, (B) porosity is retained with **2** upon sulfation of **1**, as confirmed by N_2 sorption, and (C) particle morphology was preserved after sulfation, as seen from SEM imaging.

a method to modulate active site reactivity, albeit with structural ambiguity.^{1–4}

Herein, we report the sulfated analogue of a mesoporous, 8-connected *csq* Zr_6 -MOF, NU-1000 (**1**, $[\text{Zr}_6(\mu_3\text{-O})_4(\mu_3\text{-OH})_4(\text{OH})_4(\text{H}_2\text{O})_4](\text{TBAPy})_2$, $\text{TBAPy}^+ = 1,3,6,8\text{-tetrakis-(p-benzoate)pyrene}$, Figure 1),⁵⁴ referred to as Zr-NU-1000- SO_4 -130 °C (**2**). Enhanced Brønsted acidity of **2** compared to the parent material **1** was observed and supported by a combination of spectroscopic and computational techniques. Through SCXRD, structural progression of the sulfate binding motif in analogues of **2** via sequential hydration or dehydration was monitored and identified. Sulfated MOF **2**, having undergone thermal evacuation, possessed a tridentate sulfate incorporated within the Zr_6 node via bonding at the $\mu_3\text{-OH}$ position and vicinal Zr sites. This structure, characterized by SCXRD, among other techniques, is analogous to the tripodal sulfate binding motif that has been proposed as a major species on sulfated zirconia. Finally, with the sulfated MOF structure defined, the behavior of this model system in SOMC is demonstrated through chemisorption of an organoiridium complex onto **2**. This composite is characterized and benchmarked for stoichiometric C–H bond activation and H/D exchange catalysis.

RESULTS AND DISCUSSION

Optimization of Sulfation Conditions and Confirmation of Structural Integrity. Following synthesis of **1** using a previously reported procedure (see the Supporting Information, page S17),⁵⁴ dilute H_2SO_4 (*aq*)^{46–53,55} concentrations

(0.05 M, **2**; 0.005 M, **3**; 0.1 M, **4**; 1.0 M, **5**) were screened, with minimal light exposure,⁵⁶ to achieve maximum sulfate per Zr_6 node loading (see the Supporting Information, pages S17–S21 for detailed procedures). Crystallinity was retained in the isolated MOF powders **2**, **3**, **4**, and **5**, as evidenced by PXRD patterns matching those of the parent MOF **1** (Figure 2, S11). Nitrogen adsorption/desorption isotherms showed retention of mesoporosity in the sulfated MOFs with a negligible reduction in the Brunauer–Emmett–Teller (BET) area upon sulfation, even when using concentrations as high as 1.0 M H_2SO_4 (*aq*) (see the Supporting Information, pages S22–S32). To quantify the sulfur content, **2**–**5** were digested and analyzed by inductively coupled plasma-optical emission spectroscopy (ICP-OES). Higher concentrations (**2**, **4**, and **5**) of H_2SO_4 (*aq*) all resulted in approximately 2 sulfates per Zr_6 node and sulfur wt % loadings ranging from 2.46 wt % S to 2.57 wt % S, on average (see the Supporting Information, pages S34–S37). A lower concentration (**3**) of H_2SO_4 (*aq*) led to approximately 1.36 sulfates per Zr_6 node (Table S12) and 1.8 wt % S, on average.

Thus, sulfation conditions to generate **2** were deemed optimal for maximizing crystallinity, porosity, and sulfate loading. Particle morphology was also preserved in **2**, as demonstrated in scanning electron microscopy (SEM) images of the sulfated MOF in comparison to that of **1** (Figure 2). Analysis of the pore size distribution also revealed slight reductions in cumulative pore volumes (cm^3/g) of the MOF, attributed to the installation of sulfate on the node (see the Supporting Information pages S22–S32 for further discus-

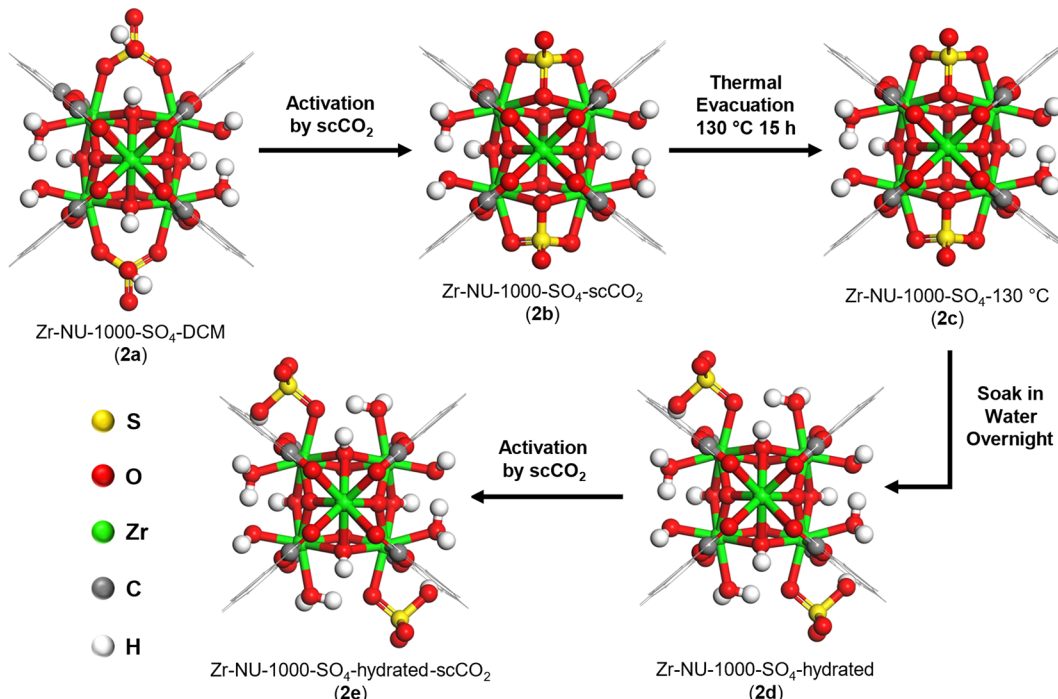


Figure 3. Structural evolution of **2** experimentally captured by SCXRD and further elucidated using DFT, resulting in the optimized geometries above. Removal of the solvent by scCO_2 caused a binding shift from bidentate (**2a**) to tridentate (**2b**) sulfate, which retains its binding motif even after thermal evacuation (**2c**). This can shift to the hydrated analogue (**2d**) upon exposure to water overnight and can be isolated using scCO_2 activation (**2e**).

sion). A significant reduction in the quantity of formate (present from adventitious decomposition of *N,N*-dimethylformamide, during solvothermal synthesis of **1**) on the node was seen after sulfation by ^1H NMR spectroscopy (see the Supporting Information, pages S39–S41). This is likely due to removal of formate under the aqueous, acidic conditions required for sulfate incorporation.⁵⁷

Investigation into Sulfate Binding Motifs under Varying Hydration Conditions. With the method of sulfation in hand, the binding motif and geometries of installed sulfates were next studied by SCXRD (see the Supporting Information for crystallographic details, pages S41–S43). Sulfate binding geometry was monitored at the various stages of preparation to make **2**, in order to draw possible parallels between the sulfated node structure and sulfate dynamics as a function of preparation methods and hydration levels on sulfated zirconia's properties (see the Supporting Information for synthesis and sulfation conditions, pages S17–S21).^{20–32,37–41}

In the freshly prepared Zr-NU-1000-SO₄ single crystals suspended in DCM (**2a**), one crystallographically independent SO₄²⁻ moiety was resolved in an asymmetric unit along the *c*-pore with four sites of positional disorder that correlated with two perpendicular mirror planes. The deposited SO₄²⁻ species on the Zr₆ node was bound in a bidentate fashion via two terminal oxygen (O_{terminal}) atoms of SO₄²⁻, while the other two oxygen atoms were directed into the *c*-pore of the MOF. This SO₄²⁻ species was pseudotetrahedral geometry, with the S–O_{terminal} bond length found to be 1.53(9) Å. The sulfur occupancies were 0.25, which is equivalent to a total loading of two SO₄²⁻ per Zr₆ node, calculated from two crystallographically equivalent sites.

With the structural orientation identified in the solvated case of **2a**, attention was next turned to evolution of the sulfate

structure upon desolvation (Figure 3). As such, DCM was removed from **2a** through sequential treatments with liquid and supercritical carbon dioxide (scCO₂) to preserve crystallinity and morphology and generate dry, solvent-free single crystals of **2b** for analysis by SCXRD (Figure 3).⁵⁸ In **2b**, two crystallographically resolved SO₄²⁻ sites were observed with two instances of positional disorder in the *c*-pore of the MOF and the mesopore, with sulfate occupancies of 0.11 and 0.08, respectively. The total quantity of SO₄²⁻ loaded onto the MOF by SCXRD was approximately one per Zr₆ node, which was lower than that which was obtained from ICP-OES measurements (2.37 SO₄²⁻ per Zr₆ node, Table S15). This discrepancy could arise for several reasons, including a nonuniform distribution of sulfate from a single crystal to single crystal due to slower diffusion or difficulties in resolution of sulfate on the MOF node due to disorder (see the Supporting Information, page S44 for a full discussion).

The local environment of the anchored SO₄²⁻ species on the Zr₆ node in **2b** changed during processing of the materials with scCO₂ to remove the DCM solvent. It was found that the deposited SO₄²⁻ species had a tridentate binding motif to the Zr₆ node, where it was bound to two O_{terminal} atoms in addition to a bridging μ_3 -O moiety (Figure 3). Notably, this configuration resembles the tripodal sulfate binding motif proposed as a major contributor to sulfate speciation on SO₄/ZrO₂ (Scheme 2A) and appears following drying, a process that removed the adventitious water necessary to stabilize the bidentate sulfate binding in **2a**. Indeed, tridentate sulfate was persistent upon further drying, and the local geometry of sulfate was retained at the Zr₆ node (Figure 3) even after thermal evacuation of the sulfated MOF crystals at 130 °C for 15 h (**2c**, see the Supporting Information for more details on drying protocols). The total SO₄²⁻ loading by SCXRD was found to be around 1.6 S per Zr₆ node with an occupancy of

0.21 for the sulfur atom. The distance between the S atom and the bound O atom to the Zr_6 node was found to be 1.69(11) ($S-O_{\text{terminal}}$ bond) and 1.70(3) Å ($S-\mu_3O$ bond), respectively. Of note, as **2c** is the single crystal analogue to the powder sample **2** and possesses a similar S/Zr_6 ratio of approximately 2.35 by ICP-OES, we anticipate the sulfate binding motif to be tridentate in both cases.

Having identified the bidentate and tridentate sulfate structures in **2a**, **2b**, and **2c**, respectively, the effect of rehydration on the sulfate structure was explored crystallographically. Recalling the hygroscopic nature of SO_4^2- /ZrO₂^{20–25,30,32,37–41} which undergoes water-mediated surface events such as protonation of bound sulfate groups, the single crystals of **2c** were next soaked in water overnight at room temperature to produce the hydrated analogue **2d** (Figure 3). From SCXRD analysis of **2d**, one crystallographically resolved SO_4^{2-} site was observed along the *c*-pore with an occupancy of 0.21 for sulfur and the total loading of SO_4^{2-} species as approximately one per Zr_6 node. The deposited SO_4^{2-} species was bound to the Zr_6 node in a monodentate fashion with an $S-O_{\text{terminal}}$ bond length of 1.57(9) Å. The tetrahedral geometry was maintained through bonding with three other oxygen atoms pointed toward the *c*-pore of the MOF. Intriguingly, the putative monodentate sulfate observed in the aqueous case is more hydrated than what has been proposed to result from the reaction of tridentate sulfate with water. When scCO₂ was used to remove the aqueous solvent, **2e** (Figure 3), a monodentate sulfate geometry remained, likely stabilized by residual water left in the MOF pores. Collectively, the obtained findings allude to the loss or addition of water as the dictating sulfate structure. This hydrated analogue is also labile, as demonstrated by sulfate displacement when exposed to aqueous selenic acid (6, Table S19).

To further explore the structural evolution of sulfate in the MOF, as a function of the degree of hydration, diffuse reflectance infrared Fourier transform spectroscopy (DRIFTS) was employed.³⁹ A DRIFTS sample spectrum of **2**, collected against the background spectrum of **1** under a static, inert Ar atmosphere, was examined to visualize discrepancies more clearly (see the Supporting Information, page S47 for the KBr-referenced spectrum). Attenuation of the isolated hydroxyl ligand stretch at 3674 cm⁻¹ is observed as a negative peak concomitant with growth of a broad positive peak centered at 3651 cm⁻¹ (Figure 4). Negative peaks are also observed

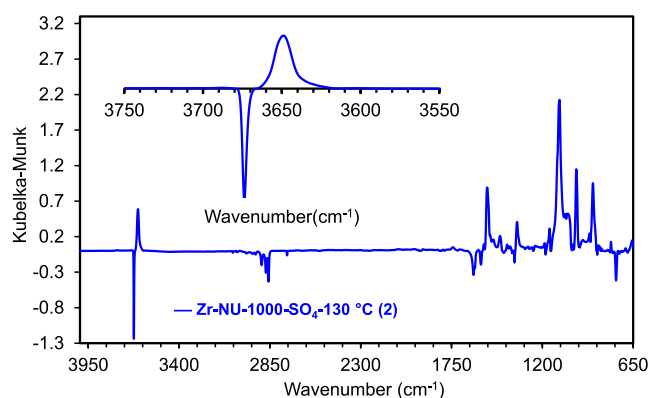


Figure 4. DRIFTS spectrum of **2** referenced against **1**, showing the emergence of new IR stretches associated with the incorporation of sulfate groups on the node.

between 2700 and 3100 cm⁻¹, which may be consistent with a decrease in the concentration of nonstructural ligands (e.g., loss of formate observed by ¹H NMR spectroscopy) on the node of **2**, likely affiliated with negative peaks at 1616 and 1575 cm⁻¹ (Figure 4). Positive peaks centered at 1532, 1350, 1098, 993, and 894 cm⁻¹ were also observed, which may correspond to the stretches associated with tridentate sulfate incorporated within the MOF node (Figure 4).

To support the sulfate hydration that was observed in **2e**, an analogous powder sample was synthesized ex-situ and examined by DRIFTS. A sample spectrum of powder **2e** (see the Supporting Information, page S48 for the KBr-referenced spectrum), collected against a background spectrum of **2**, showed a sharp, negative peak is observed at 3675 cm⁻¹ which was scrutinized further to gain insights into the –OH ligand environment (Figure 5). Peak fitting revealed the two distinct

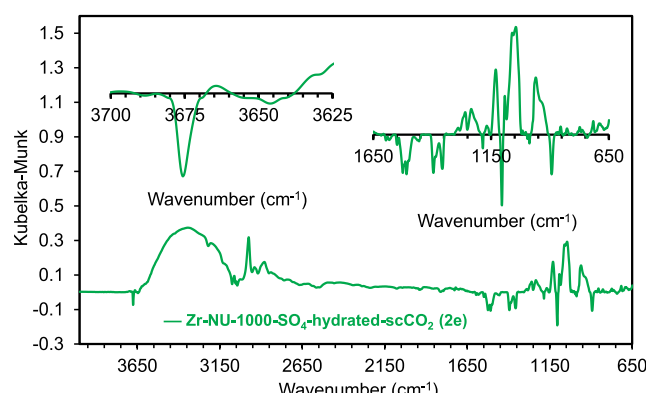


Figure 5. DRIFTS spectrum of **2e** referenced against **2**, showing the disappearance of IR stretches associated with the incorporation of sulfate groups on the node, likely due to sulfate hydration to monodentate.

features at 3675 cm⁻¹, a combination of one weak positive peak and one sharp negative peak (Figure S21, Tables S26 and S27). This may be due to superposition of multiple –OH ligand environments present in powder **2e** upon hydration (see the Supporting Information for further discussion). Evaluation of the region between 650 and 1650 cm⁻¹ reveals a mixture of positive and negative peaks that may be associated with residual ethanol (evidenced by sharp features around 1100 cm⁻¹) present in the sample and/or structural change of tridentate sulfate to monodentate or bidentate (Figure 5). Nonetheless, the broad gain peak along with a sharp loss peak in the higher frequency region certainly point toward formation of hydrated binding motifs at the expense of tridentate sulfate. The hygroscopic nature of the tridentate sulfate in the MOF was also observed in the water adsorption/desorption isotherms collected for **1** and **2**. In comparison to **1**, **2** exhibited a greater uptake of water along with a slight shift in the condensation point from $P/P_0 = 0.58$ to 0.53, indicative of this affinity for water, which could ultimately lead to geometry shifts (Figure S22).

Computational Exploration into Sulfate Geometry on the MOF Node. Density functional theory (DFT) calculations were subsequently performed to provide additional details and insights into the structural evolution of sulfated NU-1000. As is evident from the SCXRD, three different binding modes of sulfate are observed: monodentate, bidentate, and tridentate, depending on the extent of

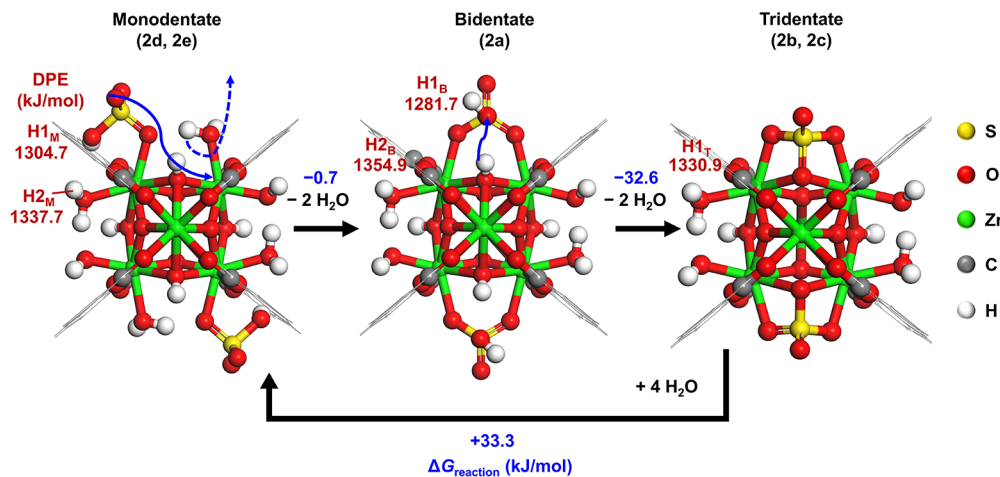


Figure 6. Structures of monodentate, bidentate, and tridentate sulfate binding motifs on the NU-1000 cluster and the calculated Gibbs free energies (ΔG) of dehydration or hydration steps. The Gibbs free energies (kJ/mol) shown in blue were calculated for experimentally observed structures that were subsequently optimized via DFT calculations. The blue arrows on the monodentate sulfate binding motif show the subsequent coordination of the sulfate to the vicinal Zr and desorption of the node-bound water. The node is shown in the ball and stick form, whereas the phenyl rings are shown in the line form for clarity. Select protons (H1_M, H2_M, H1_B, H2_B, and H1_T) are labeled in red.

hydration. DFT calculations were used to optimize each of these sulfate binding modes (Figures 6 and S31). For the monodentate binding mode observed in 2d and 2e, crystallographic characterization showed that sulfate groups were positioned either on the same face or opposite faces of the Zr-NU-1000 cluster but not on the adjacent faces. Prior literature involving $-\text{OH}_2/-\text{OH}$ groups on Zr-NU-1000 showed that a “MIX-node” configuration with $-\text{OH}_2$ and $-\text{OH}$ ligands alternating along the cluster node resulted in the most stable structure for the unmodified MOF.⁶⁰ The DFT calculations conducted herein also show that a MIX-node type configuration is favored for placement of sulfate-containing moieties in the monodentate binding case. Three candidate structures were explored with the relative orientation of the partially deprotonated HSO_4^- or fully protonated H_2SO_4 as being on (i) diagonally opposite sides of the node, (ii) opposite sides of the node, or (iii) adjacent to one another on the node (Figure S29). H_2SO_4 , being a stronger acid compared to water, preferentially binds in a dissociated fashion, with the deprotonated form as HSO_4^- -Zr and μ_3 -OH. As such, diagonally opposite positioning of bisulfates generates the lowest energy monodentate structure because it allows both groups to stay in the form of HSO_4^- (i.e., dissociatively adsorbed), while still permitting the more stable MIX-node configuration (Figure 6). The DFT-calculated S-O_{terminal} bond length, where O_{terminal} is bound to Zr, is 1.55 Å, in close agreement with the one obtained from SCXRD, 1.57(9) Å. In the bidentate case, we find that there are two HSO_4^- groups, one on either face of the inorganic node (Figure 6). Each bidentate sulfate is bound to two Zr sites in a bridged fashion via two of the oxygen atoms with S in the center and two additional oxygen atoms as S=O and S-OH respectively. The most stable structure has the S-OH group interacting via a hydrogen bond to μ_3 -OH on the node (see Figure S30 for additional bidentate candidate structures). For the O atoms that bridge the connection between S and Zr, the S-O bond lengths obtained from DFT calculations are 1.49 and 1.50 Å, also in good agreement with the 1.53(9) Å value obtained from SCXRD. For the tridentate sulfate binding motif assumed to exist in 2, 2b, and 2c, it is found that the S atom forms a bond

with the more basic μ_3 -O atom, which is typically protonated as μ_3 -OH when H_2O dissociatively adsorbs onto Zr- μ_3 -O pair sites (Figure 6). Moreover, two of the three oxygen atoms attached to the sulfur atom interact with the Lewis acidic Zr atoms, resulting in SO₃ groups bound on the Zr-O-Zr faces. In this case, SO₃ can be thought of as an analogue to dehydrated H_2SO_4 , a scenario also invoked for sulfated zirconia. The distances between the S atom and the bound O atoms to the Zr₆ node were calculated to be 1.52 (S-O_{terminal} bonds) and 1.60 Å (S- μ_3 O bond), respectively, in line with the values obtained from SCXRD, 1.69(11) Å for the S-O_{terminal} bond and 1.70(3) Å for the S- μ_3 O bond. In all three prospective structures shown in Figure 6, the structural characteristics deduced by DFT are consistent with SCXRD and spectroscopic characterization of 2a, 2b, 2c, 2d, and 2e after accounting for the partial occupancies and thermal/structural disorders.

The monodentate, bidentate, and tridentate sulfate structures are proposed to interconvert into one another by hydration or dehydration steps. Accordingly, the reaction energies were calculated for these water-mediated steps at a temperature of 298 K and water partial pressure of 0.018 atm, the latter corresponding to a relative humidity of approximately 60% (Figure 6 and Table S28). Starting from the monodentate sulfate binding mode, the desorption of two water molecules (one per Zr-O-Zr face), followed by the binding and rearrangement of HSO_4^- , results in the bidentate sulfate binding mode, with a marginal change in Gibbs free energy of $\Delta G = -0.7$ kJ/mol. This is suggestive of an equilibrium between the monodentate and bidentate sulfate motifs, with the latter being a metastable intermediate that exists in DCM solvent (2a), prior to drying. Next, the hydroxyl group of the bridged HSO_4^- in the bidentate binding mode may abstract a proton from μ_3 -OH, to liberate a water molecule, which subsequently can desorb and make way for sulfur to bind onto μ_3 -O, resulting in the dehydrated, tridentate sulfate. The favorable reaction free energy of $\Delta G = -32.6$ kJ/mol for this step suggests that the tridentate binding configuration is the most thermodynamically favorable structure under ambient humidity at 298 K.

Experimental Assessment of Brønsted Acidity in Tridentate Sulfate. Having corroborated the tridentate sulfate geometry in **2** as the most favorable and explored its structural progression, efforts toward benchmarking its Brønsted acidity were pursued. Phosphine-based probe molecules were considered to survey the potential acid sites that exist in **2**.^{46,47,61–63}

MOFs **1** and **2** were treated with a 0.2 M trimethylphosphine oxide (TMPO) solution in anhydrous DCM under an inert, Ar atmosphere.^{46,47,61–63} Collection of ^{31}P magic angle spinning (MAS) NMR spectra revealed the presence of residual, free TMPO at δ 32–34 ppm and qualitative differences in the acid site topologies of **1** and **2**. In the case of Zr-NU-1000, the ^{31}P MAS NMR spectrum of **1** contained two overlapping resonances centered at δ 50 and 54 ppm, which may correspond to the Brønsted or Lewis sites present in the parent material (Figures 7, S32). Examination of the

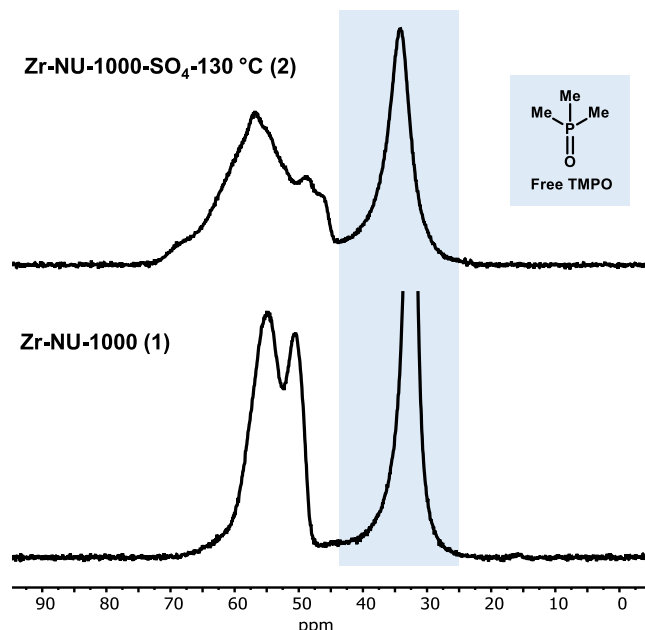


Figure 7. ^{31}P MAS NMR spectra following TMPO adsorption onto **1** (bottom) and **2** (top). A resonance associated with physisorbed TMPO was centered at δ 32–33 ppm in both materials; however an increase in ^{31}P chemical resonances occurred in **2** upon TMPO treatment, indicative of acid site formation.

corresponding spectrum for **2** revealed multiple overlapping ^{31}P resonances centered at δ 46 ppm to 69 ppm, the latter having been previously assigned to strong Brønsted acid sites in sulfated MOFs (Figures 7, S32).^{46,47}

To further elucidate the nature of the Brønsted sites present, the binding affinity of ammonia to **1** and **2** was analyzed. NH_3 adsorption/desorption isotherms were collected for the sulfated MOF and parent material at 298 K to assess the strength of interaction. Adsorption of NH_3 was examined up to 1 bar, with **2** exhibiting an uptake of 10.8 mmol/g, in contrast to 7.9 mmol/g for **1**. A closer inspection of the low-pressure region (0 to 0.0002 bar) revealed a stark difference in initial NH_3 uptake, with **2** experiencing a far steeper adsorption curve in comparison to **1** (Figure 8A,B). The sharp incline of this uptake is consistent with stronger adsorbate–adsorbent interactions being present, which may be due to chemisorption

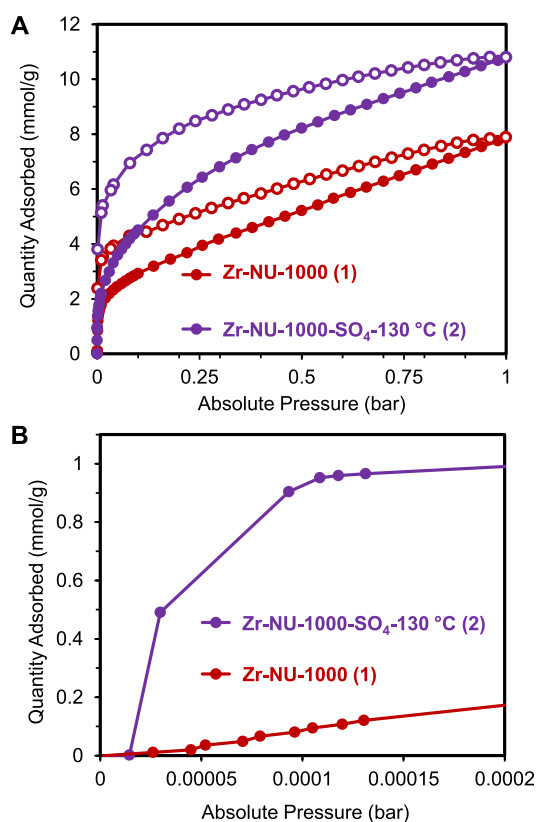


Figure 8. NH_3 adsorption/desorption isotherms at 298 K for **1** and **2** (A) and zoomed-in image into the low-pressure region to observe binding affinity (B).

of ammonia onto Brønsted acid sites in **2** and/or strong physisorption onto Lewis acid sites (Figure 8B). Indeed, when conducting three successive cycles of NH_3 sorption, identical isotherms are obtained for **1**, indicating a reversible interaction of the adsorbate (Figure S33). In contrast, for **2**, a decrease in the total uptake from 10.8 mmol/g to 9.7 mmol/g occurs between cycles 1 and 2, with a further decrease to 8.9 mmol/g in cycle 3 (Figure S34).

In an effort to deconvolute the latter point, *in situ* NH_3 DRIFTS was conducted for **1** and **2**. Evaluation of the spectra post- NH_3 treatment and evacuation for **1** and **2** resulted in significant variation in their respective IR spectra. Only small changes were observed for the parent MOF **1** (Figure 9A), whereas in the corresponding DRIFTS spectrum for **2**, an intense, broad band spanning from 2500 to 3600 cm^{-1} was observed, consistent with large quantities of ammonium present from the protonation of NH_3 by the Brønsted acid sites present in the sulfated MOF. Moving toward lower wavenumbers, two strong negative peaks are observed in the DRIFTS spectrum of **2**, at 1525 and 1392 cm^{-1} , likely stemming from interactions with node-bound sulfates and the $\text{NH}_3/\text{NH}_4^+$ adsorbates, causing changes in the chemical environment and, subsequently, IR stretch (Figure 9A). In both cases, switching to ND_3 resulted in a shift in the wavenumber, further supporting the presence of ammonium (or the deuterated analogue) in the samples (Figure 9B).

Computed Strength of Brønsted Acid Sites Upon Sulfation. There are several sources of protons in the Zr-NU-1000-SO₄ structural series (monodentate, bidentate, and tridentate). This includes the HSO₄[−] groups in the node-based monodentate (**2d** and **2e**) and bidentate (**2a**) sulfates or

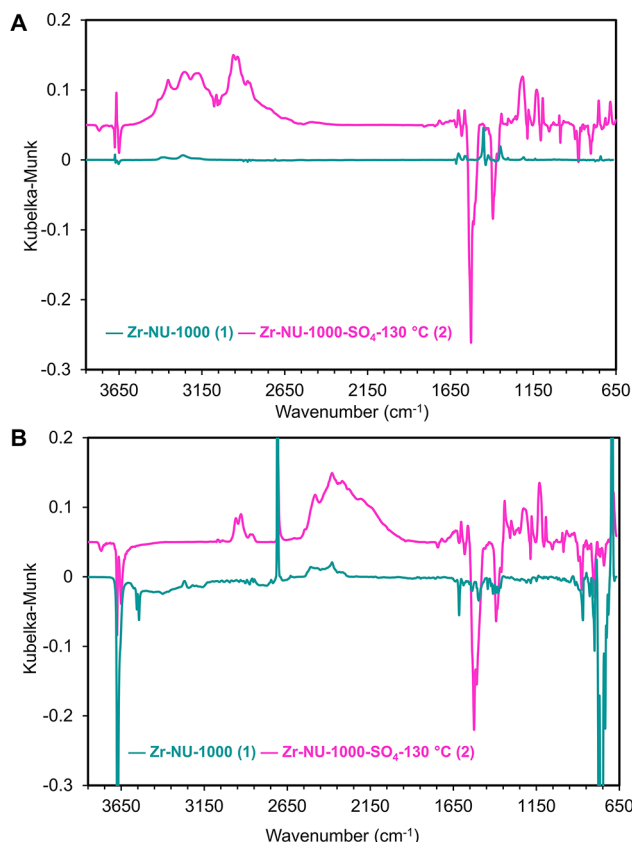


Figure 9. NH₃ in-situ DRIFTS spectra for **1** and **2** (A) and ND₃ in-situ DRIFTS spectra for **1** and **2** (B), showing that protonation of NH₃/D₃ occurs.

the adjacent water, −OH ligands, and the μ_3 −OH groups on the node. Therefore, computations were carried out to determine the acid strength for each of these and identify the strongest Brønsted acid site within the sulfated MOF materials. The deprotonation energy (DPE) was used as a measure of acidity, with a lower DPE suggesting higher acidity. Previous studies have shown that DPE values provide invaluable insights into the acid site strength and can be correlated with acid-catalyzed kinetics.^{25,64–67} Strong solid acids follow the relative order of heteropolyacids > sulfated zirconia > tungstated zirconia > zeolites, with DPE values that range from 1060–1150,^{64,65} 1160–1190,⁶⁶ 1170–1200⁶⁵ > 1220–1300 kJ/mol,⁶⁷ respectively. The calculated DPE value for sulfated zirconia of 1315 kJ/mol is somewhat higher than the value of 1165 kJ/mol estimated from kinetics of acid-catalyzed dehydration experiments.⁶⁵ The differences may arise from possible kinetic enhancements via the presence of water formed in the reaction. The DPE values for the multitude of protons in **1** and in the various structures of Zr-NU-1000-SO₄ were calculated, with a select few shown (H_{1M}, H_{2M}, H_{1B}, H_{2B}, and H_{1T}) for the monodentate (**2c** and **2d**), bidentate (**2a**), and tridentate (**2b** and **2c**) structures (Figure 6, a complete list of DPE values for all the protons is given in Figure S35). The DPE values for the Zr-NU-1000-SO₄ structures range from 1281.7 to 1363.0 kJ/mol. Notably, DPE values calculated previously for MOF-808-SO₄ were also in a similar range, 1251–1406 kJ/mol.⁴⁸ The DPE values for the assorted Zr-NU-1000-SO₄ structures are significantly lower

than those in **1** (1383.6 to 1394.9 kJ/mol), validating that the presence of sulfate groups enhances the acidity, considerably.

Overall, the Zr-bound HSO₄[−] groups observed in the bidentate sulfate configuration (**2a**) are the most acidic of all possible protons (DPE = 1281.7 kJ/mol for H_{1B}), followed by those in the monodentate sulfate configuration (**2d** and **2e**) (1304.7 kJ/mol for H_{1M}). The calculated DPE values for these Zr node-bound HSO₄[−] groups show that they are fairly acidic, with DPE values similar to those calculated for sulfated zirconia²⁵ which is a strong solid acid that demonstrates high rates for acid-catalyzed reactions.⁶³ The tridentate Zr-NU-1000-SO₄ which is the most dehydrated form among the three sulfate configurations has the most acidic protons when only the adjacent faces containing −OH₂/−OH (DPE = 1330.9 kJ/mol for H_{1T}) ligands are considered, compared to those in monodentate and bidentate Zr-NU-1000-SO₄ (DPE = 1337.7 and 1354.9 kJ/mol for H_{2M} and H_{2B}, respectively). The μ_3 −OH groups in these adjacent faces have similar DPEs to −OH₂/−OH. This latter point is significant in the context of the sulfated zirconia literature. Tripodal sulfate, analogous to tridentate sulfate in the sulfated MOF case, is thought to be a strong Lewis acid in its dehydrated state, with hydrolysis to bidentate required to generate Brønsted acid sites (Scheme 2A). However, in the case of tridentate sulfate (observed crystallographically in **2b** and **2c**), the reaction with water is not necessarily a requisite to generate strong acid sites. In fact, existing proton-bearing ligands on the surface could undergo electronic changes through close proximity to installed sulfates, thus leading to heightened acidity.

Organometallic Chemisorption of Cp*Ir(PMe₃)(Me)₂ onto Sulfated MOFs and Stoichiometric Reactivity. The stoichiometric and catalytic reactivity of the organoiridium complex, Cp*Ir(PMe₃)(Me)₂ (**7**, Cp* = 1,2,3,4,5-pentamethylcyclopentadiene), upon chemisorption was chosen as a representative probe for the effect of node sulfation on catalyst support interactions.^{33,34} It was hypothesized that anchoring the complex to the MOF node would occur via protonolysis with a surface −OH ligand, analogous to what was seen in reactions with sulfated zirconia. This grafting method involves loss of a methyl ligand from the iridium center to generate a tethered, electrophilic complex (Figure 10, Figure S63). On sulfated zirconia, this supported species was capable of rapidly activating the C–H bonds of benzene at room temperature.^{33,34}

In a J. Young NMR tube, **7** and sulfated MOF **2** (see the Supporting Information for a detailed procedure, page S75) were combined in benzene-*d*₆ and tracked by ¹H NMR spectroscopy. Immediate formation of perprotoe- and monodeuteromethane was observed contemporaneously with the conversion of **7** to Cp*Ir(PMe₃)(Me)(C₆D₅) (**8**), in addition to a decrease in the overall concentration of iridium species, which is analogous to the phenomenon observed with metal oxides (Figure 10).^{33,34} While varying degrees of C–D activation were observed at the first 20 min time point, on average, **8** accounted for 88 ± 11% of the observable organometallic speciation, with **7** accounting for the remaining 12 ± 11% (see the Supporting Information, pages S75–S77, for further discussion). By 60 min, however, **8** was the only organometallic species observed.

Liberation of perprotoemethane is due to initial protonation of Ir–Me via Brønsted acid sites on **2**, forming a reactive [Cp*Ir(PMe₃)(Me)] fragment on the sulfated node. This organometallic species is highly electrophilic and is capable of

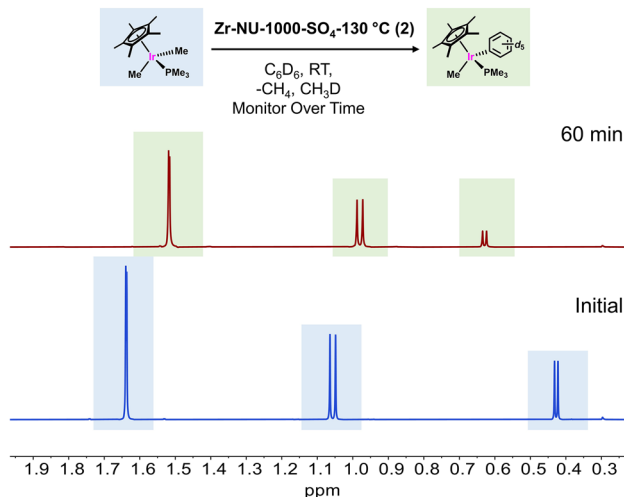


Figure 10. In situ monitoring of metalation with **7** and **2** results in C–D activation of benzene-*d*₆.

undergoing further reaction with benzene-*d*₆ in situ to generate a Cp*Ir(PMe₃) (C₆D₅) species on the sulfated MOF node (**9**), which results in evolution of monodeuteromethane in solution. The formation of **8** is an indication of the propensity of **9** to affect electrophilic C–D bond activation as this is proposed to occur by reversible dissociation of the supported organometallic species in **9**, followed by ligand exchange with residual precursor **7** left in solution. The Ir–Ph node moiety in **8** can then be regenerated by further C–D activation of benzene-*d*₆. No further reaction was observed upon continued monitoring by ¹H NMR spectroscopy of the reaction between **2** and **7**, after completion of the conversion of the residual precursor **7** to **8**. Further deuteration of generated methane was not observed, which is a departure from what has been observed for the chemisorption of **7** on sulfated zirconia and may indicate a lower electrophilicity of the Ir center on the sulfated MOF.^{33,34} Nonetheless, this stoichiometric bond activation via **9** validated the efficacy of using sulfated MOF nodes to generate electrophilic metal centers in SOMC.

Having gauged the effectiveness of **2** for chemisorption of **7**, the parent MOF **1** was next tested to validate the necessity of sulfate for the observed reactivity. Upon reacting **7** with **1** in benzene-*d*₆ (**10**), formation of perprotomethane occurs; however no C–D activation is observed by ¹H NMR spectroscopy, even after 25.5 h (Figure S39). This underscores the electrophilicity enhancement that is occurring at the Ir center when employing a sulfated MOF.

To investigate the effect of node hydration on reactivity of **7** with Zr-NU-1000-SO₄, alternative analogues were synthesized and activated using a variety of conditions to remove the solvent. In one case, scCO₂ activation was used to generate a dry, powder sample of **2b** without using heat or vacuum. Thermal evacuation was also implemented; samples of sulfated MOF activated at 250 °C (**11**) and 80 °C (**12**) for 15 h were prepared (see the Supporting Information for further discussion of synthesis and characterization). In the 250 °C case, **1** has previously been shown to undergo node dehydration when activated at 250 °C, which results in the loss of aqua-ligands from the MOF node.⁶⁰

With these materials in hand, metalation with **7** and the MOF support in benzene-*d*₆ was probed by ¹H NMR spectroscopy. In a reaction with **11**, a similar behavior was

observed to that exhibited with **2**. Quantitative conversion to **8** occurred after 20 min of exposure, with perprotomethane and monodeuteromethane observed once again (Figure S40, Table S30). In a complementary reaction with **12** and **7**, a comparable reactivity to that with **2** and **11** occurs—80 ± 17% of the product distribution is **8**, while 20 ± 17% is **7** at 20 min, which converges exclusively to **8** at 60 min (Figure S41, Table S31). Trace quantities of another species, Cp*Ir(PMe₃) (Ph) (H/D) (**13**), are also observed. After 20 min of exposure to **7** in benzene-*d*₆ using powder **2b**, 63 ± 11% of the product mixture is unreacted **7**, with 32 ± 10% corresponding to **8** and 5 ± 1% attributed to **13**. After 60 min, **7** was no longer detectable, with only **8** and **13** remaining in solution (Figure S42, Table S32). These behaviors suggest mechanistically distinct bond activation pathways being accessed as a function of node hydration.

Elucidating the Coordination Environment of Cp*Ir Organometallic Fragments on the MOF Node. Having delved into the mechanism of binding for **7** onto **2** and uncovered the in situ bond activation that results, efforts next shifted toward identifying the surface species in **9** (synthesized using perproto benzene, see the Supporting Information, page S85, for discussion of procedure for scaling up synthesis of **9**). To confirm structural integrity of **9**, a N₂ adsorption/desorption isotherm was collected at 77 K. In comparison to the porosity of **2**, a decrease is observed in the total N₂ uptake with a corresponding attenuation in the cumulative pore volume; however, mesoporosity was maintained (see the Supporting Information pages S85–S87). PXRD patterns for **9** confirmed phase purity and matches those observed for **1** and **2** (Figure S47). Furthermore, Ir loading onto the node of **2** was validated by ICP-OES, which revealed an Ir per Zr₆ loading of approximately 0.83 or 5.48 wt % Ir (Table S37). Sulfur incorporation into the node of **9** is also maintained, with the S/Zr₆ remaining approximately 2 or 2.08 wt % S (Table S37). SEM images of **9** verified that the particle size and morphology were maintained within the sample (Figure S48). Energy dispersive X-ray spectroscopy (EDS) supported a uniform distribution of sulfur and iridium within **9** (Figure S50).

The DRIFTS spectrum for **9**, referenced against **2**, possessed key changes (Figure 11A, see the Supporting Information, page S97 for the KBr-referenced spectrum). Negative peaks at 3675 and 3650 cm⁻¹ suggest protonolysis of the Ir–Me bond via –OH ligands on the node during initial chemisorption. The appearance of positive peaks between 2780 and 3070 cm⁻¹ is accordant with organic ligands remaining bound to the Ir center in **9**, thus validating their retention, following grafting onto the node of **2**. In particular, the presence of IR stretches between 3000 and 3070 cm⁻¹ supports the assignment of a putative Ir–Ph organometallic species on the node of **9**, as evidenced by absorption bands associated with aryl C–H stretching modes being present. Intriguingly, the region between 650 and 1870 cm⁻¹ shows multiple negative peaks. This may point toward sulfate moieties being influenced by the presence of Ir in **9**, causing their chemical environment to shift. To gain further insights into the nature of organic ligands bound to Ir in **9**, ¹³C cross polarization/MAS (CP/MAS) NMR spectra were collected (Figure S56). In comparing the spectra for **1** and **2**, qualitatively similar resonances are observed, although more peak broadening is present in the spectrum for **2**. When a spectrum is collected for **9**, peaks exhibited similar broadness and those present in parent MOF **2**

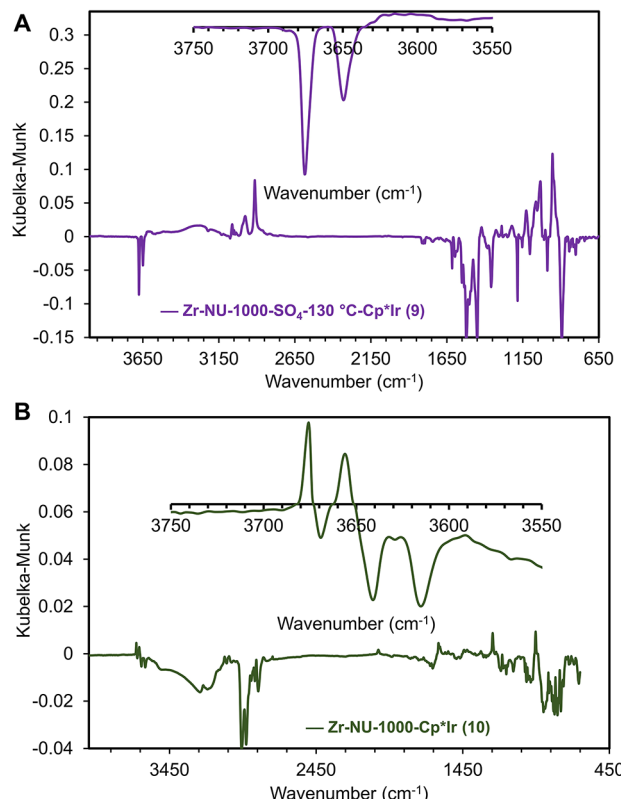


Figure 11. DRIFTS spectrum for **9** collected against **2**, showing new IR stretches associated with organoiridium chemisorption onto the MOF node (A). Similarly, the DRIFTS spectrum for **10** collected against **1** also shows emergence of new IR signatures associated with chemisorption of organoiridium.

remain. New peaks are also observed. For example, a single peak at δ 92 ppm may be consistent with the Cp* ligand bound to Ir. Notably, resonances associated with Ir–Ph are not observed; however, this may be due to overlap with peaks associated with the organic linker of the MOF. Two ^{13}C resonances at δ 13 ppm and 7.9 ppm likely correspond to the -PMe₃ ligand and methyl substituents on Cp*, respectively.

In characterizing **10**, similar structural information is obtained in the trends seen for **9**. The porosity and BET area decrease was found in the N₂ adsorption/desorption isotherm (see the Supporting Information, pages S88–S90), while crystallinity and phase purity were maintained by PXRD (Figure S47). SEM-EDS confirmed that particle morphology was maintained and showed even distribution of Ir within the sample (Figures S49 and S51). Lastly, ICP-OES corroborated Ir loading in **10**, although lower than that in **9**, with an Ir per Zr₆ loading of approximately 0.44 or 3.28 wt % Ir (Table S38).

To probe the ligand environment around Ir in **10**, DRIFTS was once again employed (Figure 11B, see the Supporting Information, page S98 for the KBr-referenced spectrum). Positive and negative peaks are observed at 3550 and 3700 cm⁻¹, possibly due to reaction of –OH ligands during chemisorption of **7** with concomitant isolation of residual –OH ligands left on the node. Interestingly, negative peaks are observed in the C–H stretching region between 2770 and 3065 cm⁻¹. This may emerge due to interactions between ligands on the Ir center with adjacent pyrene-containing linkers that could cause distortions or changes in the chemical environment. Furthermore, the ^{13}C CP/MAS NMR spectrum

of **10** (Figure S57) showed resemblance to that of **1**, in addition to resonances associated with organic ligands. The ^{13}C resonance for Cp* appeared at δ 93 ppm along with -PMe₃ at approximately δ 14 ppm and the methyl substituents of Cp* at approximately δ 8 ppm.

Because large amounts of disorders precluded characterization by SCXRD, pair distribution function (PDF) analysis was implemented to learn more about the local environment around the Ir center (Figure 12, see the Supporting

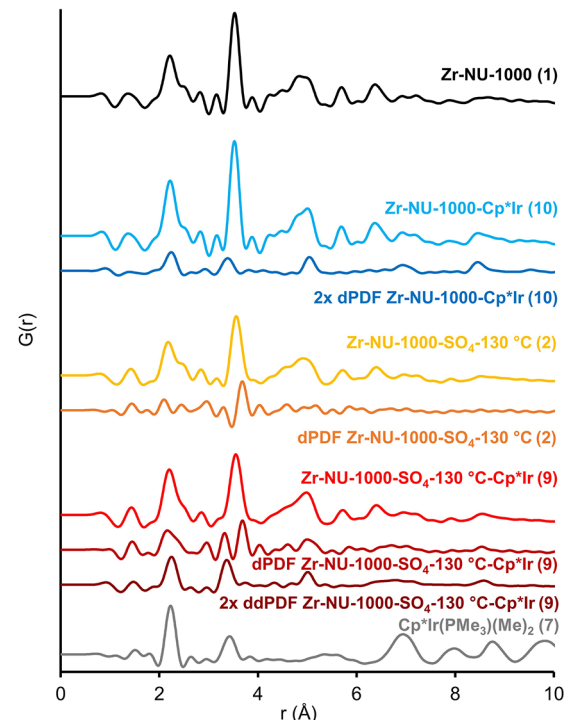


Figure 12. PDF analysis of **1**, **2**, **7**, **9**, and **10** reveals structural similarities with the presence of Ir–P/C bonds and longer range Ir…C interactions.

Information, page S99 for more information). To begin, the differential PDF (dPDF) in comparison to parent MOF **1** was first analyzed to deduce structural changes associated with the guest species. In the dPDF of **2** against **1**, a peak at 3.7 Å was present that is potentially related to the Zr–S atom pairs. In the dPDF of **10** compared to **1**, peaks at 2.2 and 3.4 Å were likely due to direct bonding between Ir and ligands in the first coordination sphere, such as Ir–C or Ir–P, whereas longer range Ir…C peaks were related to the Ir precursor **7**. More peaks at approximately 5.0, 7.0, and 8.5 Å were more likely to be atom–atom pairs between Ir and the Zr₆ node. To highlight the Ir-related peaks in **9**, a ddPDF was acquired by taking the difference between **9** and **2**. In comparing the ddPDF of **9** and dPDF of **10**, very similar peak positions are present, which points toward the tridentate SO₄²⁻ groups not impacting the local coordination environment around Ir (i.e., the PMe₃ and Cp* ligands). The Ir–node peaks in the dPDF of **9** are broader than those in **10**; however, it could be due to node distortions and/or creation of varying local structures. Overall, comparison of these PDF and dPDF features in materials containing Ir revealed similarities to the precursor **7**, supporting integrity of the ligand coordination environment around the Ir center.

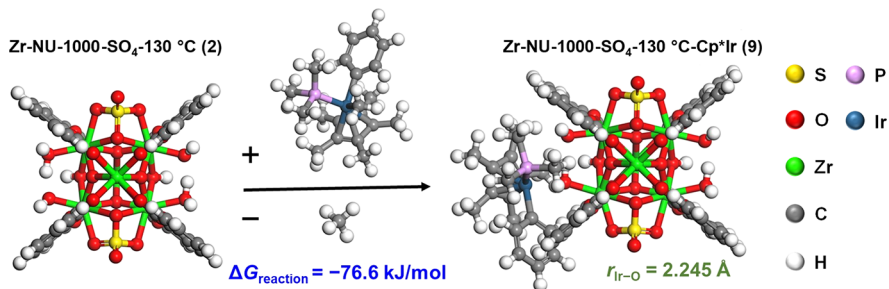


Figure 13. Cp*Ir(PMe₃)(Me)(Ph) binding on tridentate Zr-NU-1000-SO₄ (2) via protonolysis of Ir–Me and calculated Gibbs free energy (ΔG) of the reaction. The Gibbs free energy (kJ/mol) is shown in blue, and the Ir–O bonding distance is shown in green.

The electronic effect of anchoring the Ir center on the sulfated node was then investigated. ³¹P CP/MAS NMR spectra were collected to probe the extent of deshielding at the P atom attached to the Ir center (Figure S58). The ³¹P chemical shift for **9** was found to be $\delta = -26$ ppm. In contrast, the analogous ³¹P resonance in **10** appeared more upfield at $\delta = -37$ ppm, which suggests a less deshielded P atom and, as such, increased electrophilicity at the Ir center. X-ray photoelectron spectroscopy (XPS) validated the presence of Ir(III) in **9** and **10**; however, two major electronic environments were observed in the latter and one in the former (Figure S62). Subtle electronic changes were also observed for the peak positions in the Zr 3d region of the XPS spectra in comparing **9** to **10**, though changes were not observed in the P 2p region (see the Supporting Information, pages S102–S103, for further discussion of XPS).

Computational Insights into the Cp*Ir Binding Motif on the MOF Node. DFT calculations were subsequently carried out to obtain further insights into organometallic grafting on the MOF node (Figure 13). To further elucidate possible bonding mechanisms, the reactivity of aqua- and hydroxo-ligands toward the iridium organometallic precursor was evaluated using DFT (Figure S63). For simplification of the binding event, in light of observed in-situ reactivity, calculations were performed to probe grafting of perproteo **8**. In the overall reaction step, a proton from a Brønsted site in **2** reacts with a methyl ligand from **8** to liberate methane, resulting in a deprotonated, anionic binding site for the electropositive iridium complex. For binding on the more electronegative hydroxo-ligand (charge on O atom, qO = -0.67 e⁻; Figure S37), a negative Gibbs free energy of -76.6 kJ/mol was identified (Figure 13). In contrast, a free energy of -45.4 kJ/mol was calculated for **8** to bind onto the less electronegative aqua-ligand (charge on O atom, qO = -0.61 e⁻; Figure S37). This difference of 31.3 kJ/mol clearly indicates the binding preference of **8** onto the hydroxo-ligand of the node. In the optimized structure for **9**, the formed Ir–O bond length between the organometallic complex and the catalyst support is 2.25 Å.

It is worth noting that when **8** reacts with a node-bound hydroxo-ligand, proton transfer from the vicinal Zr–OH₂ to the deprotonated hydroxyl-ligand was observed, though the residence of this additional proton may be dynamic on the node (Figure S63). The above calculations on organometallic binding onto **2** are consistent with our DPE calculations for **2**. Deprotonation of a Zr–OH moiety led to a subsequent proton transfer from a vicinal water molecule back to the deprotonated oxygen atom, forming Zr–OH and resulting in a lower DPE of 1330.9 kJ/mol compared to all other DPEs

calculated for the tridentate sulfated MOF (Figure S35). The μ_3 –OH proton is also weakly acidic with a DPE of 1332.2 kJ/mol; however, our calculations show that the site is too sterically hindered to be accessible by **8** during grafting.

H/D Exchange Catalysis with Cp*Ir on the MOF Node.

Having established the stoichiometric competence of **9** for C–D bond activation and gained insights into its structure, catalytic studies were next pursued to glean insights into the relationship of sulfate to grafted Ir reactivity.⁶⁸ H/D exchange was chosen in light of the reactivity **9** exhibited with benzene-d₆, and toluene was explored as a model substrate. In a typical reaction, ~1.6 mol % (with respect to Ir) of **9** was stirred at 80 °C for 20 h in the presence of toluene in benzene-d₆, using adamantane as the internal standard. Following syringe filtration, the reaction was subsequently analyzed for exchange of protons. Gratifyingly, conversion of aromatic protons in toluene was observed using **9**, with $90 \pm 8\%$ of the *para* position exchanged, $84 \pm 11\%$ of the *meta* position exchanged, and $9 \pm 4\%$ of the *ortho* position exchanged (Table S40). Beyond exchange of the sp²-hybridized aromatic C–H bonds, deuterium incorporation was also observed at the methyl position of toluene, with $9 \pm 3\%$ exchanged. It is worth noting that the catalytic activity of **9** is lower than that for Cp*Ir on SZ (14) under analogous conditions. With **14**, 97% of the *para* position was exchanged, 96% of the *meta* position was exchanged, 94% of the *ortho* position was exchanged, and 77% of the methyl position of toluene was exchanged (Table S41), albeit with substantial background reactivity of SZ for the aromatic positions of toluene (see The Supporting Information, pages S116–S117). Nonetheless, **9** is capable of activating challenging C–H bonds, thus demonstrating its catalytic efficacy. Heterogeneity of the catalytic reaction was confirmed by a hot filtration test in which no further reactivity was observed when **9** was removed from the reaction mixture (see the Supporting Information, pages S117–S119 for details). Furthermore, integrity of the catalyst structure post-catalysis was confirmed by a N₂ adsorption/desorption isotherm (Figure S67), which proved retention of porosity, while PXRD demonstrated crystallinity and phase purity (Figure S68). Ir loading was also retained, as demonstrated by ICP-OES (Table S47). Importantly, virtually no background reactivity was observed in H/D exchange with **1** and **2** (Tables S39, S42 and S43), a departure from previous reports with ZrO₂ and SO₄/ZrO₂.^{33,34} This enables extraction of structure–activity relationships with this sulfated MOF-supported iridium catalyst without background reactivity clouding perceived trends.

Inquiring into the role of tridentate sulfate in the perceived reactivity enhancement observed with **9**, H/D exchange

catalysis was also probed for **10**. Under analogous conditions, H/D exchange was negligibly detected with **10** (Table S44).

CONCLUSIONS

In this work, we sought to create a MOF-based analogue to sulfated zirconia to better the understanding of its structure, while connecting these insights to applications in SOMC.

As such, Zr-NU-1000 was sulfated, and its structure over the course of hydration was investigated. Through a combination of SCXRD, spectroscopy, and computation, a tridentate sulfate is identified as the most dehydrated structure, whereas a monodentate sulfate is found to be the most hydrated structure. In addition, bidentate sulfate is identified as a metastable intermediate, difficult to isolate due to strong thermodynamic favorability of dehydration. To the best of our knowledge, this study represents the first in which an analogue to tripodal sulfate (invoked widely in the sulfated zirconia literature) and its hydration modes were characterized.

With the structural evidence regarding the support in hand, Brønsted acidity was benchmarked experimentally and computationally, demonstrating that sulfate incorporation led to enhancements in proton donor ability. Finally, this well-defined support was employed for immobilization of organometallic complexes that were shown to be active for stoichiometric C–D/H activation and catalytic H/D exchange. Notably, only the organoiridium complex supported on the sulfated MOF was found to exhibit bond activation in a stoichiometric and catalytic fashion, exemplifying a key structure–activity relationship operant in this system.

ASSOCIATED CONTENT

Supporting Information

The Supporting Information is available free of charge at <https://pubs.acs.org/doi/10.1021/jacs.2c05290>.

XYZ coordinates of DFT-optimized structures (ZIP)

General synthetic procedures, characterization of materials, probing Brønsted acidity, organometallic anchoring studies, and H/D exchange catalysis data (PDF)

Accession Codes

CCDC [2167212–2167215](#) and [2167521](#) contain the supplementary crystallographic data for this paper. These data can be obtained free of charge via www.ccdc.cam.ac.uk/data_request/cif, or by emailing data_request@ccdc.cam.ac.uk, or by contacting The Cambridge Crystallographic Data Centre, 12 Union Road, Cambridge CB2 1EZ, UK; fax: +44 1223 336033.

AUTHOR INFORMATION

Corresponding Authors

Massimiliano Delferro – *Chemical Sciences and Engineering Division, Argonne National Laboratory, Lemont, Illinois 60439, United States; Pritzker School of Molecular Engineering, University of Chicago, Chicago, Illinois 60637, United States;* orcid.org/0000-0002-4443-165X; Email: o-farha@u.northwestern.edu

Omar K. Farha – *Department of Chemistry and International Institute for Nanotechnology, Northwestern University, Evanston, Illinois 60208, United States;* orcid.org/0000-0002-9904-9845; Email: delferro@anl.gov

Authors

Zoha H. Syed – *Department of Chemistry and International Institute for Nanotechnology, Northwestern University, Evanston, Illinois 60208, United States; Chemical Sciences and Engineering Division, Argonne National Laboratory, Lemont, Illinois 60439, United States;* orcid.org/0000-0002-0074-2253

Mohammad Rasel Mian – *Department of Chemistry and International Institute for Nanotechnology, Northwestern University, Evanston, Illinois 60208, United States;* orcid.org/0000-0002-3034-8054

Roshan Patel – *Department of Chemical Engineering and Materials Science, University of Minnesota, Minneapolis, Minnesota 55455, United States;* orcid.org/0000-0003-4826-1536

Haomiao Xie – *Department of Chemistry and International Institute for Nanotechnology, Northwestern University, Evanston, Illinois 60208, United States;* orcid.org/0000-0001-7688-6571

Zihan Pengmei – *Department of Chemistry, Chicago Center for Theoretical Chemistry, University of Chicago, Chicago, Illinois 60637, United States*

Zhihengyu Chen – *Department of Chemistry, Stony Brook University, Stony Brook, New York 11794, United States;* orcid.org/0000-0001-5882-7076

Florencia A. Son – *Department of Chemistry and International Institute for Nanotechnology, Northwestern University, Evanston, Illinois 60208, United States;* orcid.org/0000-0002-7524-3774

Timothy A. Goetjen – *Department of Chemistry and International Institute for Nanotechnology, Northwestern University, Evanston, Illinois 60208, United States; Chemical Sciences and Engineering Division, Argonne National Laboratory, Lemont, Illinois 60439, United States;* orcid.org/0000-0001-8023-9107

Alon Chapovetsky – *Chemical Sciences and Engineering Division, Argonne National Laboratory, Lemont, Illinois 60439, United States*

Kira M. Fahy – *Department of Chemistry and International Institute for Nanotechnology, Northwestern University, Evanston, Illinois 60208, United States;* orcid.org/0000-0001-6490-3004

Fanrui Sha – *Department of Chemistry and International Institute for Nanotechnology, Northwestern University, Evanston, Illinois 60208, United States;* orcid.org/0000-0001-8310-147X

Xingjie Wang – *Department of Chemistry and International Institute for Nanotechnology, Northwestern University, Evanston, Illinois 60208, United States;* orcid.org/0000-0002-5802-9944

Selim Alayoglu – *Center for Catalysis and Surface Science, Northwestern University, Evanston, Illinois 60208, United States*

David M. Kaphan – *Chemical Sciences and Engineering Division, Argonne National Laboratory, Lemont, Illinois 60439, United States;* orcid.org/0000-0001-5293-7784

Karena W. Chapman – *Department of Chemistry, Stony Brook University, Stony Brook, New York 11794, United States;* orcid.org/0000-0002-8725-5633

Matthew Neurock – *Department of Chemical Engineering and Materials Science, University of Minnesota, Minneapolis, Minnesota 55455, United States;* orcid.org/0000-0003-1458-7837

Laura Gagliardi — Department of Chemistry, Chicago Center for Theoretical Chemistry, University of Chicago, Chicago, Illinois 60637, United States; Pritzker School of Molecular Engineering, University of Chicago, Chicago, Illinois 60637, United States;  orcid.org/0000-0001-5227-1396

Complete contact information is available at:
<https://pubs.acs.org/10.1021/jacs.2c05290>

Author Contributions

The manuscript was written through contributions of all authors. All authors have given approval to the final version of the manuscript.

Funding

The authors acknowledge support from the Inorganometallic Catalyst Design Center, an EFRC funded by the DOE, Office of Science, Basic Energy Sciences (DE-SC0012702). This work made use of the IMSERC NMR facility at Northwestern University, which has received support from the Soft and Hybrid Nanotechnology Experimental (SHyNE) Resource (NSF ECCS-2025633), Int. Institute of Nanotechnology, and Northwestern University for the a600, the Soft and Hybrid Nanotechnology Experimental (SHyNE) Resource (NSF ECCS-2025633), NSF CHE-1048773, and Northwestern University for the au400, in addition to the Soft and Hybrid Nanotechnology Experimental (SHyNE) Resource (NSF ECCS-2025633), Int. Institute of Nanotechnology, and Northwestern University for the hg400. This work made use of the EPIC facility of Northwestern University's NU Center, which has received support from the SHyNE Resource (NSF ECCS-2025633), the IIN, and Northwestern's MRSEC program (NSF DMR-1720139). DRIFTS measurements were conducted at the REACT Facility of Northwestern University Center for Catalysis and Surface Science, which is supported by a grant from the DOE (DE-SC0001329). This work also made use of the Keck-II facility of Northwestern University's NUANCE Center, which has received support from the SHyNE Resource (NSF ECCS-2025633), the IIN, and Northwestern's MRSEC program (NSF DMR-1720139). This work made use of the IMSERC Crystallography facility at Northwestern University, which has received support from the Soft and Hybrid Nanotechnology Experimental (SHyNE) Resource (NSF ECCS-2025633), and Northwestern University. Metal analysis was performed at the Northwestern University Quantitative Bio-element Imaging Center. This research also used resources of the Advanced Photon Source, a U.S. DOE Office of Science User Facility operated for the DOE Office of Science by Argonne National Laboratory under contract no. DE-AC02-06CH11357. Computational resources, in part, were provided by the Minnesota Supercomputing Institute at the University of Minnesota, and the Research Computing Center at the University of Chicago. Z.H.S. and K.M.F. are supported by the National Science Foundation Graduate Research Fellowship under Grant No. DGE-1842165. R.P. acknowledges the support of the Nanoporous Materials Genome Center, funded by the U.S. Department of Energy, Office of Basic Energy Sciences, under Award DE-FG02-17ER16362, as part of the Computational Chemical Sciences Program. F.A.S. is supported by the Department of Defense (DoD) through the National Defense Science & Engineering Graduate (NDSEG) Fellowship Program. F.A.S. and K.M.F. also acknowledge support from the Ryan Fellowship and the International Institute for Nanotechnology

at Northwestern University. T.A.G. acknowledges the support of the U.S. DOE, Office of Science, Office of Workforce Development for Teachers and Scientists, Office of Science Graduate Student Research (SCGSR) program. The SCGSR program is administered by the Oak Ridge Institute for Science and Education (ORISE) for the DOE, and ORISE is managed by ORAU under Contract DE-SC0014664.

Notes

The authors declare no competing financial interest.

ACKNOWLEDGMENTS

The authors thank Huy Nguyen for assistance with DFT of sulfated MOFs, Dr. Xuan Zhang for preliminary X-ray diffraction data collection, Dr. Ryan Witzke for providing sulfated zirconia, Dr. Yuyang Wu for assistance with solid state NMR, Rebecca Sponenburg for assistance with ICP-OES, and Dr. Timur Islamoglu for helpful discussion.

REFERENCES

- (1) Witzke, R. J.; Chapovetsky, A.; Conley, M. P.; Kaphan, D. M.; Delferro, M. Nontraditional Catalyst Supports in Surface Organometallic Chemistry. *ACS Catal.* **2020**, *10*, 11822–11840.
- (2) Copéret, C.; Chabanais, M.; Petroff Saint-Arroman, R.; Basset, J.-M. Homogeneous and Heterogeneous Catalysis: Bridging the Gap through Surface Organometallic Chemistry. *Angew. Chem., Int. Ed.* **2003**, *42*, 156–181.
- (3) Copéret, C.; Comas-Vivas, A.; Conley, M. P.; Estes, D. P.; Fedorov, A.; Mougel, V.; Nagae, H.; Núñez-Zarur, F.; Zhizhko, P. A. Surface Organometallic and Coordination Chemistry toward Single-Site Heterogeneous Catalysts: Strategies, Methods, Structures, and Activities. *Chem. Rev.* **2016**, *116*, 323–421.
- (4) Copéret, C.; Fedorov, A.; Zhizhko, P. A. Surface Organometallic Chemistry: Paving the Way Beyond Well-Defined Supported Organometallics and Single-Site Catalysis. *Catal. Lett.* **2017**, *147*, 2247–2259.
- (5) Ahn, H.; Marks, T. J. Supported Organometallics. Highly Electrophilic Cationic Metallocene Hydrogenation and Polymerization Catalysts Formed via Protonolytic Chemisorption on Sulfated Zirconia. *J. Am. Chem. Soc.* **1998**, *120*, 13533–13534.
- (6) Ahn, H.; Nicholas, C. P.; Marks, T. J. Surface Organozirconium Electrophiles Activated by Chemisorption on “Super Acidic” Sulfated Zirconia as Hydrogenation and Polymerization Catalysts. A Synthetic, Structural, and Mechanistic Catalytic Study. *Organometallics* **2002**, *21*, 1788–1806.
- (7) Williams, L. A.; Guo, N.; Motta, A.; Delferro, M.; Fragalà, I. L.; Miller, J. T.; Marks, T. J. Surface structural-chemical characterization of a single-site d0 heterogeneous arene hydrogenation catalyst having 100% active sites. *Proc. Natl. Acad. Sci. U.S.A.* **2013**, *110*, 413–418.
- (8) Gu, W.; Stalzer, M. M.; Nicholas, C. P.; Bhattacharyya, A.; Motta, A.; Gallagher, J. R.; Zhang, G.; Miller, J. T.; Kobayashi, T.; Pruski, M.; Delferro, M.; Marks, T. J. Benzene Selectivity in Competitive Arene Hydrogenation: Effects of Single-Site Catalyst... Acidic Oxide Surface Binding Geometry. *J. Am. Chem. Soc.* **2015**, *137*, 6770–6780.
- (9) Kaphan, D. M.; Ferrandon, M. S.; Langeslay, R. R.; Celik, G.; Wegener, E. C.; Liu, C.; Niklas, J.; Poluektov, O. G.; Delferro, M. Mechanistic Aspects of a Surface Organovanadium(III) Catalyst for Hydrocarbon Hydrogenation and Dehydrogenation. *ACS Catal.* **2019**, *9*, 11055–11066.
- (10) Syed, Z. H.; Kaphan, D. M.; Perras, F. A.; Pruski, M.; Ferrandon, M. S.; Wegener, E. C.; Celik, G.; Wen, J.; Liu, C.; Dogan, F.; Goldberg, K. I.; Delferro, M. Electrophilic Organoiridium(III) Pincer Complexes on Sulfated Zirconia for Hydrocarbon Activation and Functionalization. *J. Am. Chem. Soc.* **2019**, *141*, 6325–6337.
- (11) Szeto, K. C.; Loges, B.; Merle, N.; Popoff, N.; Quadrelli, A.; Jia, H.; Berrier, E.; De Mallmann, A.; Delevoye, L.; Gauvin, R. G.; Taoufik, M. Vanadium Oxo Organometallic Species Supported on

- Silica for the Selective Non-oxidative Dehydrogenation of Propane. *Organometallics* **2013**, *32*, 6452–6460.
- (12) Conley, M. P.; Delley, M. F.; Núñez-Zarur, F.; Comas-Vives, A.; Copéret, C. Heterolytic Activation of C-H Bonds on CrIII-O Surface Sites Is a Key Step in Catalytic Polymerization of Ethylene and Dehydrogenation of Propane. *Inorg. Chem.* **2015**, *54*, 5065–5078.
- (13) Sheludko, B.; Cunningham, M. T.; Goldman, A. S.; Celik, F. E. Continuous-Flow Alkane Dehydrogenation by Supported Pincer-Ligated Iridium Catalysts at Elevated Temperatures. *ACS Catal.* **2018**, *8*, 7828–7841.
- (14) Szeto, K. C.; Jones, Z. R.; Merle, N.; Rios, C.; Gallo, A.; Le Quemener, F.; Delevoye, L.; Gauvin, R. M.; Scott, S. L.; Taoufik, M. A. A Strong Support Effect in Selective Propane Dehydrogenation Catalyzed by $\text{Ga}(i\text{-Bu})_3$ Grafted onto γ -Alumina and Silica. *ACS Catal.* **2018**, *8*, 7566–7577.
- (15) Docherty, S. R.; Rochlitz, L.; Payard, P.-A.; Copéret, C. Heterogeneous alkane dehydrogenation catalysts investigated via a surface organometallic chemistry approach. *Chem. Soc. Rev.* **2021**, *50*, 5806–5822.
- (16) Millot, N.; Soignier, S.; Santini, C. C.; Baudouin, A.; Basset, J.-M. Synthesis, Characterization, and Activity in Ethylene Polymerization of Silica Supported Cationic Cyclopentadienyl Zirconium Complexes. *J. Am. Chem. Soc.* **2006**, *128*, 9361–9370.
- (17) Tafazolian, H.; Culver, D. B.; Conley, M. P. A Well-Defined Ni(II) α -Diimine Catalyst Supported on Sulfated Zirconia for Polymerization Catalysis. *Organometallics* **2017**, *36*, 2385–2388.
- (18) Culver, D. B.; Tafazolian, H.; Conley, M. P. A Bulky Pd(II) α -Diimine Catalyst Supported on Sulfated Zirconia for the Polymerization of Ethylene and Copolymerization of Ethylene and Methyl Acrylate. *Organometallics* **2018**, *37*, 1001–1006.
- (19) Rodriguez, J.; Conley, M. P. Ethylene Polymerization Activity of $(\text{R}_3\text{P})\text{Ni}(\text{codH})^+$ ($\text{cod} = 1,5\text{-cyclooctadiene}$) Sites Supported on Sulfated Zirconium Oxide. *Inorg. Chem.* **2021**, *60*, 6946–6949.
- (20) Bensitel, M.; Saur, O.; Lavallee, J.-C.; Morrow, B. A. An infrared study of sulfated zirconia. *Mater. Chem. Phys.* **1988**, *19*, 147–156.
- (21) Arata, K.; Eley, D. D.; Pines, H.; Weisz, P. B. Solid Superacids. *Adv. Catal.* **1990**, *37*, 165–211 Academic Press: Cambridge, MA.
- (22) Yamaguchi, T. Recent progress in solid superacid. *Appl. Catal.* **1990**, *61*, 1–25.
- (23) Clearfield, A.; Serrette, G. P. D.; Khazi-Syed, A. H. Nature of hydrous zirconia and sulfated hydrous zirconia. *Catal. Today* **1994**, *20*, 295–312.
- (24) Fraenkel, D. Structure of Sulfated Metal Oxides and Its Correlation with Catalytic Activity. *Ind. Eng. Chem. Res.* **1997**, *36*, 52–59.
- (25) Haase, F.; Sauer, J. The Surface Structure of Sulfated Zirconia: Periodic ab Initio Study of Sulfuric Acid Adsorbed on $\text{ZrO}_2(101)$ and $\text{ZrO}_2(001)$. *J. Am. Chem. Soc.* **1998**, *120*, 13503–13512.
- (26) Ghenciu, A.; Fărcașiu, D. The Mechanism of Conversion of Hydrocarbons on Sulfated Metal Oxides. Part II. Reaction of Benzene on Sulfated Zirconia [1]. *J. Mol. Catal. A: Chem.* **1996**, *109*, 273–283.
- (27) Drago, R. S.; Kob, N. Acidity and Reactivity of Sulfated Zirconia and Metal-Doped Sulfated Zirconia. *J. Phys. Chem. B* **1997**, *101*, 3360–3364.
- (28) Yadav, G. D.; Nair, J. J. Sulfated zirconia and its modified versions as promising catalysts for industrial processes. *Microporous Mesoporous Mater.* **1999**, *33*, 1–48.
- (29) Tanabe, K.; Hölderich, W. F. Industrial application of solid acid-base catalysts. *Appl. Catal., A* **1999**, *181*, 399–434.
- (30) Arata, K. Preparation of Superacidic Metal Oxides and Their Catalytic Action. *Metal Oxide Catalysis*; Wiley-VCH Verlag GmbH & Co. KGaA, 2009; pp 665–704.
- (31) Reddy, B. M.; Patil, M. K. Organic Syntheses and Transformations Catalyzed by Sulfated Zirconia. *Chem. Rev.* **2009**, *109*, 2185–2208.
- (32) Yan, G. X.; Wang, A.; Wachs, I. E.; Baltrusaitis, J. Critical review on the active site structure of sulfated zirconia catalysts and prospects in fuel production. *Appl. Catal., A* **2019**, *572*, 210–225.
- (33) Kaphan, D. M.; Klet, R. C.; Perras, F. A.; Pruski, M.; Yang, C.; Kropf, A. J.; Delferro, M. Surface Organometallic Chemistry of Supported Iridium(III) as a Probe for Organotransition Metal-Support Interactions in C-H Activation. *ACS Catal.* **2018**, *8*, 5363–5373.
- (34) Klet, R. C.; Kaphan, D. M.; Liu, C.; Yang, C.; Kropf, A. J.; Perras, F. A.; Pruski, M.; Hock, A. S.; Delferro, M. Evidence for Redox Mechanisms in Organometallic Chemisorption and Reactivity on Sulfated Metal Oxides. *J. Am. Chem. Soc.* **2018**, *140*, 6308–6316.
- (35) Jin, T.; Yamaguchi, T.; Tanabe, K. Mechanism of acidity generation on sulfur-promoted metal oxides. *J. Phys. Chem.* **1986**, *90*, 4794–4796.
- (36) Gillespie, R. J. Fluorosulfuric acid and related superacid media. *Acc. Chem. Res.* **1968**, *1*, 202–209.
- (37) Morterra, C.; Cerrato, G.; Bolis, V. Lewis and Brønsted acidity at the surface of sulfate-doped ZrO_2 catalysts. *Catal. Today* **1993**, *17*, 505–515.
- (38) Morterra, C.; Cerrato, G.; Pinna, F.; Signoretto, M. Brosted Acidity of a Superacid Sulfate-Doped ZrO_2 System. *J. Phys. Chem.* **1994**, *98*, 12373–12381.
- (39) Katada, N.; Endo, J.-I.; Notsu, K.-I.; Yasunobu, N.; Naito, N.; Niwa, M. Superacidity and Catalytic Activity of Sulfated Zirconia. *J. Phys. Chem. B* **2000**, *104*, 10321–10328.
- (40) Babou, F.; Coudurier, G.; Vedrine, J. C. Acidic Properties of Sulfated Zirconia: An Infrared Spectroscopic Study. *J. Catal.* **1995**, *152*, 341–349.
- (41) Hino, M.; Kurashige, M.; Matsuhashi, H.; Arata, K. The surface structure of sulfated zirconia: Studies of XPS and thermal analysis. *Thermochim. Acta* **2006**, *441*, 35–41.
- (42) Rosenberg, D. J.; Bachiller-Baeza, B.; Dines, T. J.; Anderson, J. A. Nature of Surface Sulfate Species and the Generation of Active Sites on Silica–Zirconia Mixed-Oxide Catalysts. *J. Phys. Chem. B* **2003**, *107*, 6526–6534.
- (43) Wasson, M. C.; Buru, C. T.; Chen, Z.; Islamoglu, T.; Farha, O. K. Metal-organic frameworks: A tunable platform to access single-site heterogeneous catalysts. *Appl. Catal., A* **2019**, *586*, 117214.
- (44) Syed, Z. H.; Sha, F.; Zhang, X.; Kaphan, D. M.; Delferro, M.; Farha, O. K. Metal-Organic Framework Nodes as a Supporting Platform for Tailoring the Activity of Metal Catalysts. *ACS Catal.* **2020**, *10*, 11556–11566.
- (45) Liu, J.; Goetjen, T. A.; Wang, Q.; Knapp, J. G.; Wasson, M. C.; Yang, Y.; Syed, Z. H.; Delferro, M.; Notestein, J. M.; Farha, O. K.; Hupp, J. T. MOF-enabled confinement and related effects for chemical catalyst presentation and utilization. *Chem. Soc. Rev.* **2022**, *S1*, 1045–1097.
- (46) Jiang, J.; Gándara, F.; Zhang, Y.-B.; Na, K.; Yaghi, O. M.; Klemperer, W. G. Superacidity in Sulfated Metal-Organic Framework-808. *J. Am. Chem. Soc.* **2014**, *136*, 12844–12847.
- (47) Trickett, C. A.; Osborn Popp, T. M.; Su, J.; Yan, C.; Weisberg, J.; Huq, A.; Urban, P.; Jiang, J.; Kalmutzki, M. J.; Liu, Q.; Baek, J.; Head-Gordon, M. P.; Somorjai, G. A.; Reimer, J. A.; Yaghi, O. M. Identification of the strong Brønsted acid site in a metal-organic framework solid acid catalyst. *Nat. Chem.* **2019**, *11*, 170–176.
- (48) Yang, B.; Wheeler, J. I.; Sorensen, B.; Steagall, R.; Nielson, T.; Yao, J.; Mendez-Arroyo, J.; Ess, D. H. Computational determination of coordination structure impact on adsorption and acidity of pristine and sulfated MOF-808. *Mater. Adv.* **2021**, *2*, 4246–4254.
- (49) Jiang, J.; Yaghi, O. M. Brønsted Acidity in Metal-Organic Frameworks. *Chem. Rev.* **2015**, *115*, 6966–6997.
- (50) Feng, L.; Wang, Y.; Yuan, S.; Wang, K.-Y.; Li, J.-L.; Day, G. S.; Qiu, D.; Cheng, L.; Chen, W.-M.; Madrahimov, S. T.; Zhou, H.-C. Porphyrinic Metal-Organic Frameworks Installed with Brønsted Acid Sites for Efficient Tandem Semisynthesis of Artemisinin. *ACS Catal.* **2019**, *9*, 5111–5118.
- (51) Otake, K.-I.; Ye, J.; Mandal, M.; Islamoglu, T.; Buru, C. T.; Hupp, J. T.; Delferro, M.; Truhlar, D. G.; Cramer, C. J.; Farha, O. K. Enhanced Activity of Heterogeneous Pd(II) Catalysts on Acid-Functionalized Metal-Organic Frameworks. *ACS Catal.* **2019**, *9*, 5383–5390.

- (52) Fernández-Morales, J. M.; Lozano, L. A.; Castillejos-López, E.; Rodríguez-Ramos, I.; Guerrero-Ruiz, A.; Zamaro, J. M. Direct sulfation of a Zr-based metal-organic framework to attain strong acid catalysts. *Microporous Mesoporous Mater.* **2019**, *290*, 109686.
- (53) Goesten, M. G.; Juan-Alcañiz, J.; Ramos-Fernandez, E. V.; Sai Sankar Gupta, K. B.; Stavitski, E.; van Bekkum, H.; Gascon, J.; Kapteijn, F. Sulfation of metal-organic frameworks: Opportunities for acid catalysis and proton conductivity. *J. Catal.* **2011**, *281*, 177–187.
- (54) Islamoglu, T.; Otake, K.-I.; Li, P.; Buru, C. T.; Peters, A. W.; Akpinar, I.; Garibay, S. J.; Farha, O. K. Revisiting the structural homogeneity of NU-1000, a Zr-based metal-organic framework. *CrystEngComm* **2018**, *20*, 5913–5918.
- (55) 95–98% sulfuric acid was used in all node sulfation procedures. For determining the molar ratio of sulfuric acid to node during functionalization, the median value of 96.5% sulfuric acid was used for calculations.
- (56) Due to the inherent photochemical properties of Zr-NU-1000, all manipulations were conducted with minimal exposure to ambient light to preclude its impact on reactivity.
- (57) Lu, Z.; Liu, J.; Zhang, X.; Liao, Y.; Wang, R.; Zhang, K.; Lyu, J.; Farha, O. K.; Hupp, J. T. Node-Accessible Zirconium MOFs. *J. Am. Chem. Soc.* **2020**, *142*, 21110–21121.
- (58) Nelson, A. P.; Farha, O. K.; Mulfort, K. L.; Hupp, J. T. Supercritical Processing as a Route to High Internal Surface Areas and Permanent Microporosity in Metal–Organic Framework Materials. *J. Am. Chem. Soc.* **2009**, *131*, 458–460.
- (59) Li, B.; Gonzalez, R. D. An in situ DRIFTS study of the deactivation and regeneration of sulfated zirconia. *Catal. Today* **1998**, *46*, 55–67.
- (60) Planas, N.; Mondloch, J. E.; Tussupbayev, S.; Borycz, J.; Gagliardi, L.; Hupp, J. T.; Farha, O. K.; Cramer, C. J. Defining the Proton Topology of the Zr₆-Based Metal-Organic Framework NU-1000. *J. Phys. Chem. Lett.* **2014**, *5*, 3716–3723.
- (61) Zheng, A.; Huang, S.-J.; Chen, W.-H.; Wu, P.-H.; Zhang, H.; Lee, H.-K.; de Ménorval, L.-C.; Deng, F.; Liu, S.-B. 31P Chemical Shift of Adsorbed Trialkylphosphine Oxides for Acidity Characterization of Solid Acids Catalysts. *J. Phys. Chem. A* **2008**, *112*, 7349–7356.
- (62) Zheng, A.; Huang, S.-J.; Liu, S.-B.; Deng, F. Acid properties of solid acid catalysts characterized by solid-state 31P NMR of adsorbed phosphorous probe molecules. *Phys. Chem. Chem. Phys.* **2011**, *13*, 14889–14901.
- (63) Bornes, C.; Fischer, M.; Amelse, J. A.; Geraldes, C. F. G. C.; Rocha, J.; Mafra, L. What Is Being Measured with P-Bearing NMR Probe Molecules Adsorbed on Zeolites? *J. Am. Chem. Soc.* **2021**, *143*, 13616–13623.
- (64) Janik, M. J.; Macht, J.; Iglesia, E.; Neurock, M. Correlating Acid Properties and Catalytic Function: A First-Principles Analysis of Alcohol Dehydration Pathways on Polyoxometalates. *J. Phys. Chem. C* **2009**, *113*, 1872–1885.
- (65) Macht, J.; Carr, R. T.; Iglesia, E. Functional assessment of the strength of solid acid catalysts. *J. Catal.* **2009**, *264*, 54–66.
- (66) Zhou, W.; Soultanidis, N.; Xu, H.; Wong, M. S.; Neurock, M.; Kiely, C. J.; Wachs, I. E. Nature of Catalytically Active Sites in the Supported WO₃/ZrO₂ Solid Acid System: A Current Perspective. *ACS Catal.* **2017**, *7*, 2181–2198.
- (67) Jones, A. J.; Carr, R. T.; Zones, S. I.; Iglesia, E. Acid strength and solvation in catalysis by MFI zeolites and effects of the identity, concentration and location of framework heteroatoms. *J. Catal.* **2014**, *312*, 58–68.
- (68) Quantification of H/D exchange by ¹H NMR of the aromatic positions of toluene may be impacted by overlapping satellite signals with the peaks of interest in the NMR spectra. Nonetheless, we anticipate the impact of these satellite signals to be minor on the % exchange values reported.

□ Recommended by ACS

Synthetic Access to a Framework-Stabilized and Fully Sulfided Analogue of an Anderson Polyoxometalate that is Catalytically Competent for Reduction Reactions

Jiaxin Duan, Joseph T. Hupp, et al.

MARCH 22, 2023

JOURNAL OF THE AMERICAN CHEMICAL SOCIETY

READ ▶

Nonclassical Strong Metal–Support Interactions for Enhanced Catalysis

Yifan Sun, Sheng Dai, et al.

FEBRUARY 27, 2023

THE JOURNAL OF PHYSICAL CHEMISTRY LETTERS

READ ▶

Structure and Site Evolution of Framework Ni Species in MIL-127 MOFs for Propylene Oligomerization Catalysis

Benjamin Yeh, Aditya Bhan, et al.

FEBRUARY 01, 2023

JOURNAL OF THE AMERICAN CHEMICAL SOCIETY

READ ▶

Structure–Activity Relationship Insights for Organophosphonate Hydrolysis at Ti(IV) Active Sites in Metal–Organic Frameworks

Mohammad Rasel Mian, Omar K. Farha, et al.

MARCH 15, 2023

JOURNAL OF THE AMERICAN CHEMICAL SOCIETY

READ ▶

Get More Suggestions >